

Magnetism and spin dynamics of an $S = 3/2$ frustrated trillium lattice antiferromagnet $\text{K}_2\text{CrTi}(\text{PO}_4)_3$

J. Khatua,^{1,2} Suheon Lee,³ Gyungbin Ban,² Marc Uhlarz,⁴ Kwang-Yong Choi,^{2,*} and P. Khuntia^{1,5,†}

¹*Department of Physics, Indian Institute of Technology Madras, Chennai 600036, India*

²*Department of Physics, Sungkyunkwan University, Suwon 16419, Republic of Korea*

³*Center for Artificial Low Dimensional Electronic Systems,*

Institute for Basic Science, Pohang 37673, Republic of Korea

⁴*Dresden High Magnetic Field Laboratory (HLD-EMFL),*

Helmholtz-Zentrum Dresden-Rossendorf, 01328 Dresden, Germany

⁵*Quantum Centre of Excellence for Diamond and Emergent Materials,*
Indian Institute of Technology Madras, Chennai 600036, India.

(Dated: January 25, 2024)

Competing magnetic interactions, frustration-driven quantum fluctuations, and spin-correlation offer an ideal route for the experimental realization of emergent quantum phenomena and exotic quasi-particle excitations in three-dimensional frustrated magnets. In this context, trillium lattice, wherein magnetic ions decorate a three-dimensional chiral network of corner-shared equilateral triangular motifs, provides a viable ground. Herein, we present the crystal structure, magnetic susceptibility, specific heat, electron spin-resonance (ESR), muon spin-relaxation (μSR) results on the polycrystalline samples of $\text{K}_2\text{CrTi}(\text{PO}_4)_3$ wherein the Cr^{3+} ions form a perfect trillium lattice without any detectable anti-site disorder. The Curie-Weiss fit of the magnetic susceptibility data above 100 K yields a Curie-Weiss temperature $\theta_{\text{CW}} = -23$ K, which indicates the presence of dominant antiferromagnetic interactions between $S = 3/2$ moments of Cr^{3+} ions. The specific heat measurements reveal the occurrence of two consecutive phase transitions, at temperatures $T_{\text{L}} = 4.3$ K and $T_{\text{H}} = 8$ K, corresponding to two different magnetic phases. Additionally, it unveils the existence of short-range spin correlations above the ordering temperature T_{H} . The power-law behavior of ESR linewidth suggests the persistence of short-range spin correlations over a relatively wide critical region $(T - T_{\text{H}})/T_{\text{H}} > 0.25$ in agreement with the specific heat results. The μSR results provide concrete evidence of two different phases corresponding to two transitions, coupled with the critical slowing down of spin fluctuations above T_{L} and persistent spin dynamics below T_{L} , consistent with the thermodynamic results. Moreover, the μSR results reveal the coexistence of static and dynamic local magnetic fields below T_{L} , signifying the presence of complex magnetic phases owing to the entwining of spin correlations and competing magnetic interactions in this three-dimensional frustrated magnet.

I. INTRODUCTION

Frustrated quantum materials, where competing interactions between localized spin moments and frustration-induced strong quantum fluctuations prevent classical Néel order, are highlighted as promising contenders for the discovery of emergent physical phenomena such as quantum spin liquid (QSL), and spin ice with exotic excitations that goes beyond conventional symmetry breaking paradigms in condensed matter [1–4].

A QSL state is a highly entangled state, in which frustration-induced strong quantum fluctuations defy long-range magnetic order even at absolute zero temperatures, despite strong exchange coupling between magnetic moments in the host spin-lattice [5–9]. Instead, two spins in the corresponding lattice form resonating spin-singlet pairs or long-range entangled states with exotic fractionalized excitations such as spinons coupled to emergent gauge fields [10]. Experimental realization

of fractional quantum numbers, their identification and interaction are of profound importance in elucidating the underlying mechanism of some of the groundbreaking phenomena such as high-temperature superconductivity, fractional Hall effect, topological spin-textures, and monopoles in quantum condensed matter [11–18] that could have far-reaching ramifications in both fundamental physics and innovative quantum technologies [16]. The realization of QSL state is well established in one-dimensional magnets, however, its identification in higher dimensional spin system remains a long-standing challenge in modern condensed matter physics.

In the quest of this long-sought goal, significant effort has been devoted to the exploration of two-dimensional (2D) frustrated lattices [4], which has led to the identification of a few QSL candidates in 2D systems [19, 20]. Meanwhile, three-dimensional (3D) frustrated spin-lattices such as hyperkagome and pyrochlore lattice are found to host QSL as well. Despite the fact that quantum fluctuations are less pronounced in 3D lattices, certain frustrated 3D lattices, including transition metal-based hyperkagome lattices $\text{PbCuTe}_2\text{O}_6$ [21, 22] and $\text{Na}_4\text{Ir}_3\text{O}_8$ [23, 24] along with pyrochlore lattice $\text{NaCaNi}_2\text{F}_7$ [25–27] as well as rare-earth-based pyrochlore lattice $\text{Ce}_2\text{Zr}_2\text{O}_7$

* choisky99@skku.edu

† pkhuntia@iitm.ac.in

[28], shows signatures of QSL state driven by frustration-induced strong quantum fluctuations [29]. However, the experimental realization of QSL in 3D spin lattice remains scarce, as most of the candidate materials show spin-freezing or magnetic ordering owing to perturbing terms in the spin Hamiltonian, lattice imperfections, and exchange anisotropy. In this respect, it is pertinent to investigate promising frustrated magnets on 3D spin lattices wherein competition between emergent degrees of freedom offers an alternate route to stabilize exotic quantum and topological states [4, 30–33]

To date, hexagonal-based layered frustrated magnets have been studied rigorously for their 2D QSL and certain cubic lattice systems for their 3D counterparts [34]. Recently, there is growing interest in non-centrosymmetric frustrated quantum materials which crystallize in the cubic space group $P2_13$ [35–37]. The lack of inversion symmetry in such non-centrosymmetric materials gives rise to interesting physical phenomena owing to anisotropic Dzyaloshinskii-Moriya (DM) interactions [35, 38–42]. For example, non-centrosymmetric cubic quantum materials are known to host a wide range of quantum phenomena including magnetic skyrmions in insulator $\text{Cu}_2\text{OSe}_2\text{O}_3$ [43], and in itinerant magnets MnSi [44], and FeGe [45], and topological Hall effect in MnGe [46]. Apart from quantum phenomena induced by DM interactions, the spin frustration induced quantum phenomena in such 3D non-centrosymmetric chiral magnets have garnered significant attention in the quest to achieve distinct quantum phenomena. It is observed that in such quantum materials that crystallizes in the cubic structure ($P2_13$) the magnetic ions form a trillium lattice i.e., a 3D chiral network of corner-shared equilateral triangular motifs which provides the origin of spin frustration and may host a myriads of frustration-induced physical phenomena such as QSL. It is a well known that a geometrically frustrated lattice has the potential to harbor frustration-induced new quantum phenomena, as observed in intermetallic compounds. Notable examples include the presence of a dynamic state above the transition temperature in $\text{EuPt}(\text{Si}/\text{Ge})$ [47], a spin-ice-like state in CeIrSi [48], and the occurrence of pressure-induced quantum phase transitions in MnSi [49].

Nevertheless, oxide-based materials having a single trillium lattice structure are extremely rare. Recently, the trillium lattice, composed of corner-sharing equilateral triangles with six nearest neighbors, has emerged as an alternative route to further explore the influence of quantum fluctuations in the 3D QSL state and to realize unique quantum phenomena [37, 50]. Remarkably, a recent study on the langbeinite family member $\text{K}_2\text{Ni}_2(\text{SO}_4)_3$, which crystallizes in a cubic ($P2_13$) crystal structure, reveals that Ni^{2+} ($S = 1$) ions form a coupled trillium lattice [51]. This material demonstrates several magnetic sublattices with competing magnetic interactions and exhibits a 3D QSL state induced by an applied magnetic field [51]. More recently, continuum spin excitations driven by strong quantum fluctu-

ations are revealed by inelastic neutron scattering measurement on single crystals of $\text{K}_2\text{Ni}_2(\text{SO}_4)_3$ [52]. Furthermore, despite possessing a high spin moment, the signature of a spin-liquid state has been observed in the trillium compounds $\text{KSrFe}_2(\text{PO}_4)_3$ (Fe^{3+} ; $S = 5/2$) [53] and $\text{Na}[\text{Mn}(\text{HCOO})_3]$ (Mn^{2+} ; $S = 5/2$) [54], that invokes further investigation of the ground state and associated quasi-particle excitations in analogous trillium lattice antiferromagnets. In addition, the spin correlations, interplay between competing interactions and the topology of the electronic band structure in non-centrosymmetric magnets stabilizing in 3D spin lattice make them an exciting class of materials with potential technological applications [55, 56].

Herein, we focus on a new phosphate langbeinite $\text{K}_2\text{CrTi}(\text{PO}_4)_3$ (henceforth KCTPO), wherein Cr^{3+} ions with $S = 3/2$ form a trillium lattice without any detectable anti-site disorder between constituent atoms. Magnetization data reveals the presence of dominant antiferromagnetic interactions between $S = 3/2$ moments of Cr^{3+} ions. Specific heat measurements demonstrate two magnetic transitions, namely at $T_L = 4.3$ K and $T_H = 8$ K, as well as the development of short-range spin correlations above T_H , which is supported by critical-like behavior of the ESR line width. Furthermore, μSR data uncovers an intriguing evolution of static and dynamic spin correlations, notably below T_L , and a critical slowing down of spin dynamics above T_L . Our experimental findings reveal a complex magnetic landscape with coexisting states, successive phase transitions, and dynamic behavior of Cr^{3+} moments decorating a frustrated 3D trillium spin-lattice over a wide temperature regime.

II. EXPERIMENTAL DETAILS

Polycrystalline samples of KCTPO were prepared by a conventional solid-state reaction method. The appropriate stoichiometric amounts of K_2CO_3 (Alfa Aesar, 99.997 %), Cr_2O_3 (Alfa Aesar, 99.97 %), TiO_2 (Alfa Aesar, 99.995 %) and $(\text{NH}_4)_2\text{HPO}_4$ (Alfa Aesar, 98 %) were mixed. Prior to use, the reagent K_2CO_3 was preheated in air at 100°C to eliminate moisture. The stoichiometric mixture was pelletized, and the pellet was sintered at 300°C for 4 hrs. This sintering procedure was repeated at several intermediate temperatures before annealing the sample at 800°C for 48 hrs to achieve a single-phase composition. Powder x-ray diffraction (XRD) data were collected using a smartLAB Rigaku x-ray diffractometer with Cu K_α radiation ($\lambda = 1.54 \text{ \AA}$) at room temperature.

Magnetization measurements were performed using the VSM option of Physical Properties Measurement System (PPMS, Quantum Design) in the temperature range of $2 \text{ K} \leq T \leq 300 \text{ K}$ and in magnetic fields up to 7 T. Specific heat measurements were performed using PPMS by thermal relaxation method in the temperature range of $1.9 \text{ K} \leq T \leq 250 \text{ K}$ and in magnetic fields up to 7

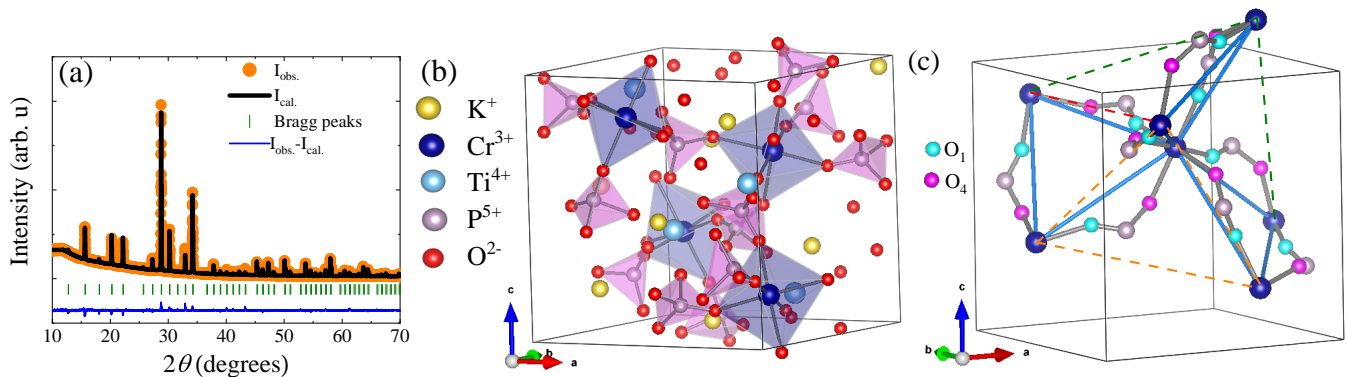


FIG. 1. (a) Rietveld refinement pattern of the room temperature powder x-ray diffraction data of $\text{K}_2\text{CrTi}(\text{PO}_4)_3$. The orange circle, black line, olive vertical bars, and blue line show the experimentally observed points, the result of Rietveld fitting, expected Bragg reflection positions, and the difference between observed and calculated intensities, respectively. (b) Schematic depicting the one unit cell of $\text{K}_2\text{CrTi}(\text{PO}_4)_3$. The Cr^{3+} ions form distorted CrO_6 octahedra (blue), and the P^{5+} ions form PO_4 tetrahedra (pink). These are connected through a shared oxygen ion, resulting in the formation of a Cr-O-P-O-Cr superexchange bridge with nearest CrO_6 octahedra. (c) The nearest-neighbor Cr^{3+} ions (solid blue line; 6.10 Å) arrange themselves in a trillium lattice, featuring six nearest neighbors. Trillium lattice is composed of three motifs of equilateral triangle of Cr^{3+} ions with possible nearest-neighbor superexchange routes. The second (8.32 Å), third (9.79 Å), and fourth (10.06 Å) nearest neighbors are shown by the dashed orange, red, and olive lines, respectively. Other atoms are omitted to ensure a clearer view of the trillium lattice and potential nearest-neighbor exchange paths.

T. High-field magnetization measurement was conducted at Dresden High Magnetic Field Laboratory, sweeping a magnetic field up to 30 T at 4 K using a nondestructive pulsed magnet. The obtained data were scaled to the isothermal magnetization taken with PPMS at 4 K.

X-band ($\nu = 9.5$ GHz) electron spin resonance (ESR) measurements were performed using a Bruker EMXplus-9.5/12/P/L spectrometer with a continuous He flow cryostat in the temperature range of $4 \text{ K} \leq T \leq 300 \text{ K}$. The $\mu^+\text{SR}$ experiments in zero field and in weak transverse magnetic field (32 G) were performed at the surface muon beamline M20 at TRIUMF in the temperature range $1.93 \text{ K} \leq T \leq 80 \text{ K}$. Powder samples (approximately 0.5 g) were placed into a thin envelope composed of Mylar tape coated with aluminum ($\sim 50 \mu\text{m}$ thick), which was mounted on a Cu fork sample stick. A standard ^4He flow cryostat was employed to achieve the base temperature of 1.93 K for TRIUMF/M20. The obtained μSR data was analyzed using the *musrfit* software package [57].

III. RESULTS

A. Rietveld refinement and crystal structure

In order to ensure phase purity and determine atomic parameters of the polycrystalline samples of KCTPO, the Rietveld refinement of powder XRD data was performed using GSAS software [58]. For the Rietveld refinement, the initial atomic parameters were obtained from references [59–61]. The Rietveld refinement reveals that KCTPO crystallizes in a cubic space group ($P2_13$) and the resulting refinement pattern is shown in Fig. 1 (a).

No secondary phase was found, confirming the successful synthesis of KCTPO in its single phase. The observed sharp and well-defined XRD peaks imply that high-quality polycrystalline samples have been used in this study. The obtained lattice parameters as well as goodness factors from the Rietveld refinement of powder XRD are tabulated in table I. Our analysis shows the absence of any detectable anti-site disorders between the atoms that constitute KCTPO.

Figure 1 (b) depicts the one unit cell of KCTPO, where Cr^{3+} ions form distorted CrO_6 octahedra with nearest-neighbor O^{2-} that are separated from adjacent CrO_6 octahedra by PO_4 tetrahedra. The bonding between the CrO_6 octahedra and TiO_4 tetrahedra through a common oxygen ion is expected to construct a 3D Cr-O-P-O-Cr superexchange pathway between two nearest-neighbor Cr^{3+} ions (see table II). Most interestingly, the nearest-neighbor Cr^{3+} ions (6.10 Å) form a trillium lattice, i.e., a 3D network of corner-shared equilateral triangular lattice with coordination number six (Fig. 1 (c)), potentially serving as a platform for hosting a frustrated spin-lattice in 3D.

From a structural point of view, KCTPO belongs to the langbeinite family $\text{K}_2\text{M}_2(\text{SO}_4)_3$ ($M = \text{Mg}, \text{Co}, \text{Ni}, \dots$), which crystallizes in the cubic crystal structure (space structure $P2_13$). Two crystallographic $4a$ sites occupy divalent magnetic ions that form a double trillium lattice in the sulfate langbeinites without any anti-site disorder [51]. Among various phosphate langbeinites, the recently reported phosphate langbeinite $\text{KSrFe}_2(\text{PO}_4)_3$ shows a similar configuration, featuring a double trillium lattice with two magnetic sites of Fe^{3+} ions and K/Sr anti-site disorder [53]. Unlike the aforementioned dou-

TABLE I. Rietveld refinement of x-ray diffraction data at 300 K yielded structural parameters of $\text{K}_2\text{CrTi}(\text{PO}_4)_3$. (Space group: $P2_13$, $a = b = c = 9.796 \text{ \AA}$, $\alpha = \beta = \gamma = 90^\circ$ and $\chi^2 = 2.86$, $R_{\text{wp}} = 5.29 \%$, $R_p = 3.56 \%$, and $R_{\text{exp}} = 1.84\%$)

Atom	Wyckoff position	x	y	z	Occ.
Cr	4a	0.666	0.666	0.666	1
K ₁	4a	0.960	0.960	0.960	1
K ₂	4a	0.186	0.186	0.186	1
Ti	4a	0.391	0.391	0.391	1
P	12b	0.474	0.703	0.368	1
O ₁	12b	0.609	0.860	0.737	1
O ₂	12b	0.463	0.314	0.232	1
O ₃	12b	0.506	0.573	0.313	1
O ₄	12b	0.585	0.721	0.457	1

TABLE II. Bond lengths and angles between atoms that result in distinct antiferromagnetic interactions between Cr^{3+} spins.

Bond length (\AA)	Bond angle ($^\circ$)
Cr-O ₁ = 2.101	\angle Cr-O ₁ -P = 153.510
Cr-O ₄ = 2.262	\angle O ₁ -P-O ₄ = 120.635
P-O ₄ = 1.405	\angle P-O ₄ -Cr = 143.804
P-O ₁ = 1.273	\angle Cr-Cr-Cr = 60
Cr-P = 3.494	\angle Cr-P-Cr = 128.355
O ₁ -O ₄ = 2.32	\angle Cr-O ₁ -Cr = 154.692

ble trillium lattice-based langbeinites, KCTPO, a phosphate langbeinite, accommodates a single magnetic site (4a) hosting Cr^{3+} ions, alongside another 4a site occupied by non-magnetic Ti^{4+} ions. This characteristic positions KCTPO as a considerably simpler 3D lattice, suited for the experimental realization of theoretically proposed physical phenomena intrinsic to the trillium lattice [36, 62].

B. Magnetic susceptibility

Figure 2 (a) depicts the temperature dependence of magnetic susceptibility $\chi(T)$ in several magnetic fields up to 7 T. Upon lowering temperature, a sharp increase of $\chi(T)$ was observed below 10 K, tending to saturate in a magnetic field $\mu_0 H = 1 \text{ T}$. This behavior indicates the presence of long-range magnetic order in KCTPO consistent with the specific heat result presented in this work. However, this behavior is suppressed significantly in magnetic fields $\mu_0 H \geq 3 \text{ T}$. A minor bump around 50 K that appeared in all magnetic fields is attributed to residual oxygen trapped in the polycrystalline sample that was wrapped with teflon during measurement [63]. This signal is not an intrinsic characteristic of the investigated compound in this study.

In order to determine the dominant magnetic interaction between the $S = 3/2$ moments of Cr^{3+} ions, the linear region ($100 \text{ K} \leq T \leq 300 \text{ K}$) of the $1/\chi(T)$ data in

a magnetic field $\mu_0 H = 1 \text{ T}$ was fitted by the Curie-Weiss (CW) law, i.e., $\chi = \chi_0 + C/(T - \theta_{\text{CW}})$. Here, χ_0 is the sum of temperature-independent core diamagnetic susceptibility (χ_{core}) and Van Vleck paramagnetic susceptibility (χ_{VV}), C is the Curie constant used to estimate the effective magnetic moment ($\mu_{\text{eff}} = \sqrt{8C} \mu_{\text{B}}$) and θ_{CW} is the Curie-Weiss temperature associated with the exchange interaction between magnetic moments of Cr^{3+} ions. The corresponding CW fit (red line in the inset of Fig. 2 (a)) yields $\chi_0 = -7.42 \times 10^{-4} \text{ cm}^3/\text{mol}$, $C = 1.88 \text{ cm}^3 \text{ K}/\text{mol}$, and $\theta_{\text{CW}} = -23 \pm 0.15 \text{ K}$. The estimated effective magnetic moment $\mu_{\text{eff}} = 3.87 \mu_{\text{B}}$, is close to the value $g\sqrt{S(S+1)} = 3.87 \mu_{\text{B}}$ expected for $S = 3/2$ moments of free Cr^{3+} ions. The negative θ_{CW} indicates the presence of dominant antiferromagnetic interactions between the $S = 3/2$ spin of Cr^{3+} ions. As depicted in the inset of Fig. 2 (a), the Curie-Weiss fit begins to diverge below 80 K, signaling the onset of antiferromagnetic spin correlations upon lowering the temperature [64]. Interestingly, the material shows anomalies at low temperatures associated with magnetic phase transitions.

To further understand the effect of magnetic fields on the long-range magnetic ordered state in KCTPO, the zero-field-cooled (ZFC) and field-cooled (FC) χ measurements were performed in weak magnetic fields $\mu_0 H \geq 0.005 \text{ T}$. Figure 2 (b) reveals the presence of a clear bifurcation between ZFC and FC χ below the temperature ($T_{\text{L}} = 4.3 \text{ K}$) in a magnetic field of $\mu_0 H = 0.005 \text{ T}$, which implies the presence of a ferromagnetic component below T_{L} . Nevertheless, as the magnetic field strength increases, the deviation between ZFC and FC magnetic susceptibility gradually diminishes, almost converging at a magnetic field $\mu_0 H = 0.05 \text{ T}$.

In order to shed more insights concerning the nature of magnetically ordered phases at different temperature regimes, isotherm magnetization measurements were performed at several temperatures as shown in the inset of Fig. 2 (c). Several features can be observed in the isotherm magnetization curves such as a weak S-shaped curvature in low-fields at 2 K, indicating the existence of a ferromagnetic component consistent with the bifurcation between ZFC and FC susceptibility below T_{L} [65–67]. Notably, the magnetization at 2 K does not reach saturation in a high magnetic field (9 T); instead, the linear behavior of the magnetization curves implies the presence of a canted antiferromagnetic state below T_{L} . A similar scenario, attributed to the canted antiferromagnetic phase, has also been observed in several frustrated magnets [68, 69]. As the temperature increases, the S-shaped curvature is gradually suppressed due to the quenching of the ferromagnetic component, finally disappearing. The resulting magnetization curve becomes linear at 10 K, indicating the crossover to an additional antiferromagnetic phase. These observations imply that KCTPO exhibits a canted antiferromagnetic state below T_{L} , above which it hosts an additional antiferromagnetic state corroborated by the specific heat results described below. To find the saturation magnetic moment in high magnetic

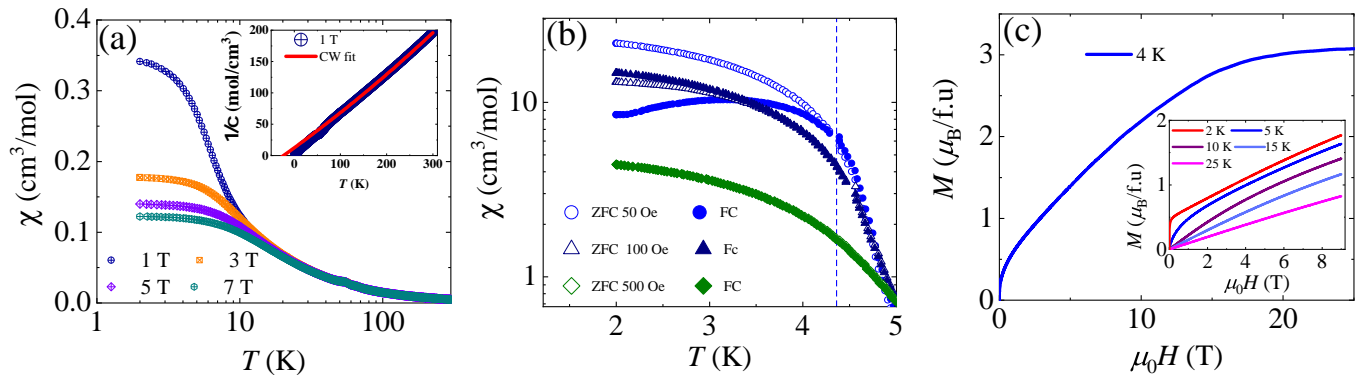


FIG. 2. (a) Temperature dependence of magnetic susceptibility, $\chi(T)$, of $\text{K}_2\text{CrTi}(\text{PO}_4)_3$ in several magnetic fields. The inset depicts the temperature dependence of inverse magnetic susceptibility at $\mu_0 H = 1$ T. The red line represents the Curie-Weiss fits to the high-temperature inverse susceptibility data. (b) Temperature dependence of zero-field cooled (ZFC) and field-cooled (FC) magnetic susceptibility in the temperature range $2 \text{ K} \leq T \leq 5 \text{ K}$ in magnetic fields $0.005 \text{ T} \leq \mu_0 H \leq 0.05 \text{ T}$. The dotted vertical line is at temperature $T_L = 4.3 \text{ K}$, below which ZFC and FC bifurcation begins in a magnetic field of $\mu_0 H = 0.005 \text{ T}$. (c) Magnetization as a function of an external magnetic field up to 30 T at 4 K. The inset shows the isotherm magnetization up to 9 T at several temperatures.

fields, magnetization measurements were performed at 4 K using a pulsed field magnet up to 30 T.

Figure 2 (c) represents the high-field magnetization data at 4 K, calibrated using the VSM-SQUID data at 4 K. It is worth to note that a weak ferromagnetic component persists in low fields $\mu_0 H \leq 0.012 \text{ T}$ and beyond this magnetic-field, the magnetization continues to increase linearly until $\mu_0 H \leq 14 \text{ T}$ and reaches a saturation magnetic moment of $3.04 \mu_B$ in 24 T. We recall that the saturation field is comparable to the CW temperature discussed above. The obtained saturation magnetic moment of $3.04 \mu_B$ is close to the expected theoretical value of $3.0 \mu_B$ per Cr^{3+} ions ($S = 3/2$). The absence of a fractional “1/3” magnetization plateau indicates either the classical behavior of Cr^{3+} spins or the presence of perturbation terms such as magnetic anisotropy and longer-range interactions [70, 71].

C. Specific heat

Specific heat is an excellent probe to track magnetic order and associated low-lying excitations in frustrated magnets. In order to discern the evidence of magnetic long-range order, temperature-dependent specific heat measurements were performed in several magnetic fields. Figure 3 (a) shows the temperature dependence of specific heat in the whole measured temperature range in zero-magnetic field. As shown in Fig. 3 (b), below $T = 10 \text{ K}$, the specific heat exhibits two anomalies: one at the temperature $T_L = 4.3 \text{ K}$ and another at the temperature $T_H = 8 \text{ K}$ in zero-magnetic field, suggesting the occurrence of successive magnetic phase transitions in KCTPO. It is worth to note that the low-temperature anomaly occurring at T_L in specific heat coincides with

the temperature below which the splitting of ZFC and FC χ (Fig. 2 (b)) as well as the appearance of a ferromagnetic component in magnetization are observed (Fig. 2 (c)). This coincidence suggests that the anomaly at T_L is most likely related to the transition temperature of the canted antiferromagnetic phase in KCTPO. On the other hand, the anomaly at $T_H = 8 \text{ K}$ is attributed to the transition temperature of additional antiferromagnetic phase of KCTPO. We recall that the two successive magnetic phase transitions are also observed in the two coupled trillium lattice $\text{K}_2\text{Ni}_2(\text{SO}_4)_3$ [51].

Figure 3 (b) displays the specific heat in several magnetic fields in the low-temperature regime. The salient observation is that the low-temperature anomaly at T_L shifts towards higher temperatures upon the application of a magnetic field, eventually vanishing at a magnetic field of $\mu_0 H = 3 \text{ T}$. The increase in T_L with increasing magnetic field can be ascribed to either strong quantum fluctuations or the presence of competing anisotropic interactions. While the applied magnetic field increases, the anomaly at T_H widens, shifts to slightly lower temperatures, and a clear λ -like anomaly is observed in $\mu_0 H = 7 \text{ T}$, suggesting the presence of a typical antiferromagnetic second-order phase transition at T_H in KCTPO. Moreover, in the temperature range $8 \text{ K} \leq T \leq 20 \text{ K}$, the specific heat exhibits field dependency, indicating that specific heat is of magnetic origin in this temperature range.

In order to estimate the magnetic entropy and understand the low-temperature magnetic properties relevant to this trillium lattice antiferromagnet, one must subtract the lattice specific heat ($C_{\text{latt}}(T)$) from the total specific heat ($C_p(T)$). To extract the lattice contributions, we used a combination of one Debye and three

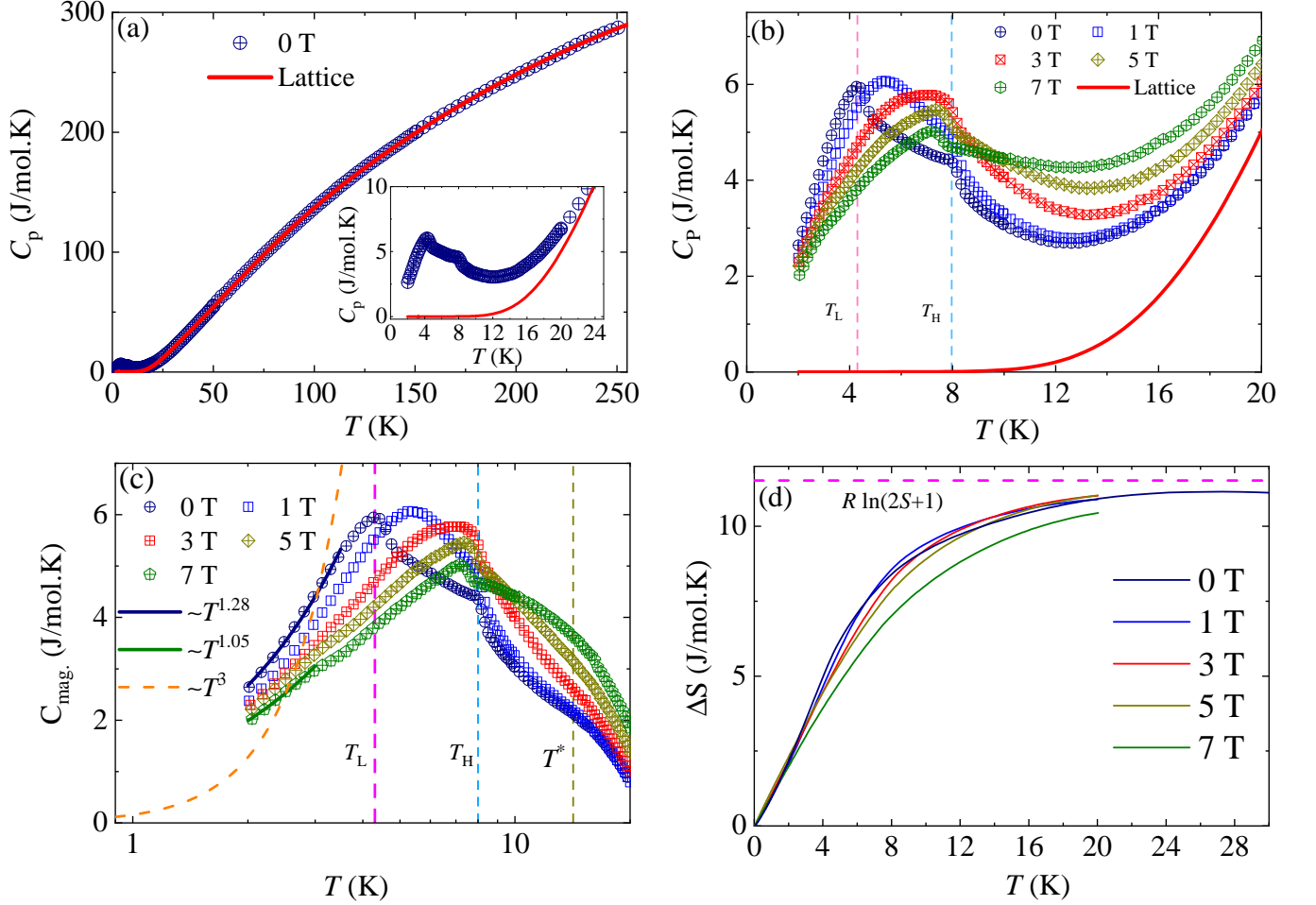


FIG. 3. (a) Temperature dependence of specific heat (C_p) of $\text{K}_2\text{CrTi}(\text{PO}_4)_3$ in zero-magnetic field. The solid red line represents the lattice contributions obtained by combining one Debye and three Einstein functions as described in text. The inset shows a closer view of the low-temperature specific heat. (b) Temperature dependence of $C_p(T)$ in several magnetic fields in the temperature range $2 \text{ K} \leq T \leq 20 \text{ K}$. The dashed vertical lines indicate two anomalies: one at temperature $T_L = 4.30 \text{ K}$ and another at temperature $T_H = 8 \text{ K}$ in zero-field. (c) Temperature dependence of $C_{\text{mag}}(T)$ in several magnetic fields in semi-log scale. Below $T_L = 4.3 \text{ K}$, the solid lines tentatively represent $\sim T^n$ power-law behavior of magnetic specific heat, where n varies from 1.3 to 1 in an applied magnetic field of 7 T. The dashed orange line represents the $C_{\text{mag}}(T) \sim T^3$ behavior typical for conventional antiferromagnets. (d) Temperature dependence of entropy change in several magnetic fields with the horizontal pink line indicating the expected entropy of $R \ln(4)$ for $S = 3/2$ spin of Cr^{3+} ions.

Einstein terms, i.e.,

$$C_{\text{latt}}(T) = C_D \left[9k_B \left(\frac{T}{\theta_D} \right)^3 \int_0^{\theta_D/T} \frac{x^4 e^x}{(e^x - 1)^2} dx \right] + \sum_{i=1}^3 C_{E_i} \left[3R \left(\frac{\theta_{E_i}}{T} \right)^2 \frac{\exp(\frac{\theta_{E_i}}{T})}{(\exp(\frac{\theta_{E_i}}{T}) - 1)^2} \right], \quad (1)$$

where θ_D is the Debye temperature, θ_{E_i} s are the Einstein temperatures of the three modes, R and k_B are the molar gas constant and Boltzmann constant, respectively. The corresponding lattice fit, yielding $\theta_D = 223 \text{ K}$, $\theta_{E_1} = 376 \text{ K}$, $\theta_{E_2} = 615 \text{ K}$, and $\theta_{E_3} = 1344 \text{ K}$, is represented by the solid red line on top of the experimental data point in

Fig. 3 (a). In order to minimize the fitting parameters, the coefficients were set at a fixed ratio of $C_D : C_{E_1} : C_{E_2} : C_{E_3} = 1 : 1 : 1.5 : 6$, closely matching with the ratio of the number of heavy atoms (K, Cr, Ti, P) to light atoms (O) in KCTPO.

After subtraction of the lattice contributions, the obtained temperature dependence of magnetic specific heat $C_{\text{mag}}(T)$ is shown in Fig. 3 (c). As the temperature decreases in a zero-magnetic field, C_{mag} increases and exhibits a broad maximum around temperature $T^* = 14 \text{ K}$, followed by a weak kink at T_H . The broad maximum is attributed to the presence of short-range spin correlations [51]. The presence of a moderate frustration parameter f , roughly estimated through the ratio $f = |\theta_{\text{CW}}|/T_H \approx 3$,

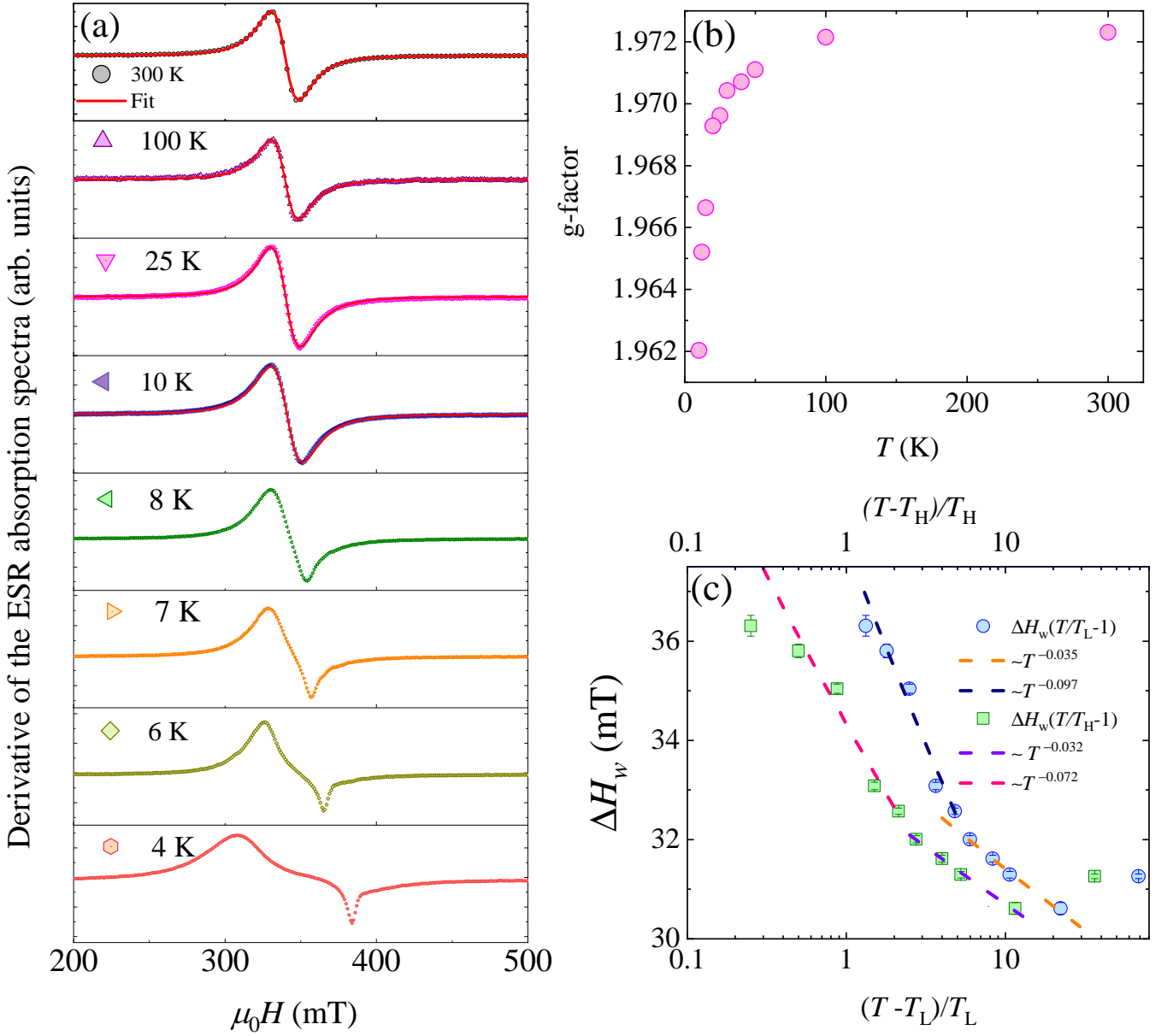


FIG. 4. (a) Derivative of the ESR absorption spectra of $\text{K}_2\text{CrTi}(\text{PO}_4)_3$ at selected temperatures. The solid red lines indicate the fitting to the Lorentzian line shape above 8 K. (b) Temperature dependence of g -factor in semi-log scale. (c) Semi-log plot of the ESR linewidth ΔH_w as a function of the reduced temperature expressed as $T_{i1} = (T - T_L)/T_L$ on the bottom x -axis and $T_{rh} = (T - T_H)/T_H$ on the upper x -axis. The dashed lines are power-law fits.

could account for both the short-range order and the suppression of magnetic order. The anomaly at T_H is relatively weak compared to the anomaly at T_L similar to the observed anomalies in $\text{K}_2\text{Ni}_2(\text{SO}_4)_3$ [51]. Nevertheless, upon increasing the magnetic field, the canted antiferromagnetic phase diminishes, leading to an increase in the anomaly observed at T_H in $\mu_0 H = 7$ T. Most notably, as shown in Fig. 3 (c), the magnetic specific heat follows $C_{\text{mag}} \sim T^n$ ($n = 1.28$) power-law in zero field for temperatures below T_L , which significantly deviates from the $C_{\text{mag}}(T) \sim T^3$ behavior typical of conventional

antiferromagnets. In the presence of a magnetic field up to 7 T, the average value of n was found to be 1.10. It is worth noting that in future low temperature specific heat measurements are required to confirm whether the power-law behavior persists even in the sub-Kelvin temperature range. In contrast to KCTPO, the trillium lattice structure with two interpenetrating sublattices of $\text{K}_2\text{Ni}_2(\text{SO}_4)_3$, well below the transition temperature, the magnetic specific heat follows $C_{\text{mag}} \sim T^2$ behavior [51].

To quantify the entropy release associated with phase transitions and spin dynamics, it is crucial to account the

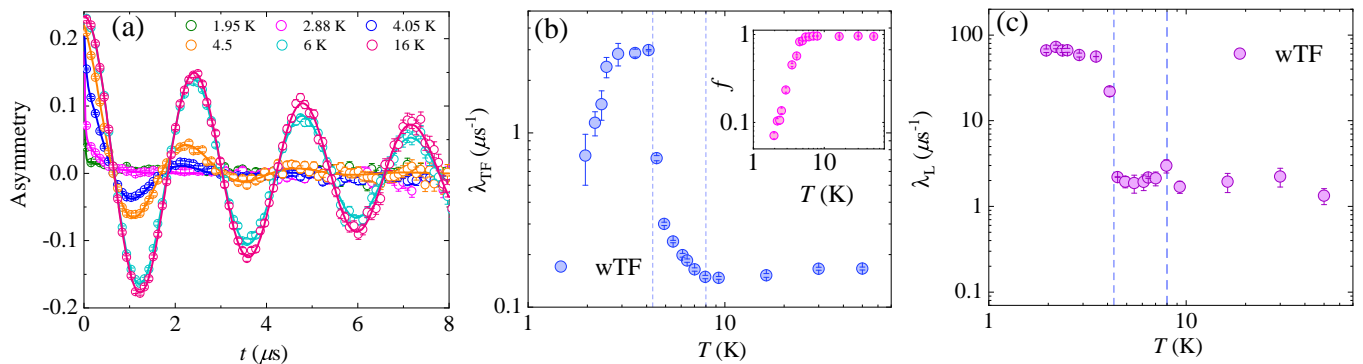


FIG. 5. (a) Time dependence of the muon asymmetry in $\text{K}_2\text{CrTi}(\text{PO}_4)_3$ in a weak transverse field ($B_{\text{TF}} = 32$ G) at a several temperatures. The solid lines are fits obtained using Eq. 2. (b) Temperature dependence of muon spin relaxation rate in transverse applied field on a double logarithmic scale. The inset shows the fraction of the oscillating component as a function of temperature. (c) Temperature dependence of muon spin relaxation rate due to internal magnetic field in the investigated sample. The dashed vertical lines indicate the position of characteristic transition temperatures at $T_L = 4.3$ K and $T_H = 8$ K.

magnetic-specific heat below 2 K. In the absence of no more phase transition below 2 K, we extend the corresponding power-law to zero temperature. Next, the entropy was obtained by integrating C_{mag}/T with respect to temperature, as shown in Fig. 3 (d). The obtained saturation entropy is found to be 11.16 J/mol·K at 30 K that is close to the theoretically expected value 11.52 J/mol·K for $S = 3/2$ moments. The missing ~ 3.12 % entropy is ascribed to either the existence of short-range magnetic correlations well above the transition temperature or an overestimation of the lattice contribution given the limitations of the model employed here [72, 73]. Additionally, around the transition temperature T_H of 8 K, approximately 76 % of the saturation entropy is released, suggesting that roughly 20 % originates from short-range spin correlations that begin forming as high as at $\sim 3T_H$. However, the lack of a few percentage of entropy because of short-range order persisting above the transition temperature is typical for frustrated magnets [64, 72]. This observation is corroborated by the ESR results presented in the following subsection.

D. Electron spin resonance

To provide microscopic insights into the temperature evolution of spin correlations, we conducted X-band ESR measurements down to 4 K [74]. The obtained ESR spectra at several temperatures are shown in Fig. 4 (a), which fits well with a derivative of a Lorentzian curve above 8 K. This indicates that the ESR signal is exchange narrowed. At temperatures below $T = 10$ K, the spectra cannot be fitted by a single Lorentzian curve, indicating the development of antiferromagnetic resonance mode and supporting the conclusions drawn from thermodynamic results. The temperature dependence of estimated g -factors from the fit is shown in Fig. 4 (b). Above $T = 100$ K, the obtained g value remains relatively constant

at approximately $g = 1.972$, slightly lower than the standard $g = 2$ for a free Cr^{3+} ion. This value is typical for a less-than-half-filled Cr^{3+} ion with a negligible spin-orbit interaction in an octahedral ligand coordination, as observed in similar compounds [73]. The g -factor starts to decrease with temperature below 100 K, which corresponds to the deviation from the CW fit (see the inset of Fig. 2 (a)). This is attributed to the persistent magnetic correlations up to several $|\theta_{\text{CW}}|$, often observed in frustrated magnets [64].

The ESR linewidth is directly proportional to the spin correlations in transition metal-based systems with minimum spin-orbit coupling. Figure 4 (c) shows the estimated ESR linewidth (ΔH_w) of KCTPO as a function of reduced temperatures $T_{rl} = (T - T_L)/T_L$ in the bottom x -axis and $T_{rh} = (T - T_H)/T_H$ in the upper x -axis. Above the transition temperature T_H , the observed linewidth exhibits a power-law behavior of $T_{rl}/T_{rh} \sim T^{-p}$ in two distinct temperature ranges. For temperatures spanning from 10 K to 24 K, the power exponent p takes values of 0.097 and 0.072, while in the range of 30 K to 100 K, the values of p are 0.035 and 0.032 for T_{rl} and T_{rh} , respectively [64, 73, 75, 76]. The critical-like broadening in the temperature range $10 \text{ K} \leq T \leq 24 \text{ K}$, alongside the weak hump at T^* in C_{mag} and the small percentage of entropy released above 8 K, supports the notion of the critical-like spin fluctuations. Conversely, the broadening observed in the temperature range of $30 \text{ K} \leq T \leq 100 \text{ K}$ is ascribed to cooperative paramagnetic behavior between the $S = 3/2$ spin of Cr^{3+} ions. Additionally, a deviation from the Curie-Weiss fit has also been noted below 100 K (refer to Fig. 2 (a)). The presence of two stage broadening is also observed in other high-spin based frustrated magnets alluding to the two-step thermal evolution of magnetic correlations [64, 75, 76].

E. Muon spin relaxation

To capture the microscopic details of spin dynamics and the internal magnetic field distribution, μ SR measurements were performed on polycrystalline samples of KCTPO in zero-field (ZF) and weak transverse field (wTF). When a weak transverse field (here $B_{\text{TF}} = 32$ G) is applied perpendicular to the initial direction of the muon spin polarization, the implanted muon spin precesses around the applied transverse field in the paramagnetic state of the sample, leading to an oscillatory signal with a frequency of $\gamma_{\mu}B_{\text{TF}}/2\pi$, where $\gamma_{\mu} = 2\pi \times 135.5$ MHz/T represents the muon gyromagnetic ratio [77]. In addition, when a static magnetic field is present in the sample, the muon spin polarization exhibits a non-oscillatory signal, as observed in the material under investigation [72, 78, 79]. Figure 5 (a) shows the evolution of the TF spectra at selected temperatures that were fitted according to

$$A_{\text{wTF}}(t) = A_0 f \cos(\gamma_{\mu} B_{\text{TF}} t + \phi) e^{-\lambda_{\text{TF}} t} + (1 - f) A_0 e^{-\lambda_L t}, \quad (2)$$

which combines an exponentially decaying oscillatory component, corresponding to muon spins experiencing zero-static field, and an exponentially decaying non-oscillatory component that accounts for the component of the static local field parallel to the initial muon polarization. In Eq. 2, A_0 represents the initial asymmetry at time zero, ϕ denotes the relative phase, λ_{TF} stands for the muon spin relaxation rate in the applied transverse field, and f quantifies the fraction of the oscillatory component while λ_L refers to the muon spin relaxation rate caused by the internal magnetic fields. At short time scales, we observe a significantly damped signal with decreasing temperature without any loss of initial asymmetry, which is a characteristic signature of a magnetically ordered state in KCTPO.

The estimated fraction of the oscillatory signal f , associated to the volume fraction experiencing zero-static field (inset of Fig. 5 (b)), remains constant to a value of 0.93 in the temperature range $4.3 \text{ K} \leq T \leq 78 \text{ K}$. This temperature independent value of $f < 1$ is attributed to the presence of weak static local fields above 4.3 K which is also observed in ESR results. However, it gradually decreases below $T_L = 4.3 \text{ K}$, indicating a crossover to another magnetically ordered state. It is noteworthy that f does not sharply drop to zero below the transition temperature T_L , suggesting the existence of dynamic local fields in the ordered state. Upon lowering the temperature, the transverse field muon spin relaxation rate gradually increases (see Fig. 5 (b)), as expected in the extreme motional narrowing limit of fluctuating magnetic moments. A sharp peak in λ_{TF} at T_L indicates the critical slowing down of spin fluctuations above the transition temperature as evident from unsaturated magnetic entropy. The notable observation is the occurrence of the critical spin relaxation below T_H [47]. Conversely, the muon spin relaxation rate caused by the static local field (Fig. 5 (c))

exhibits a weak kink at T_H , attributed to the antiferromagnetic phase transition similar to that observed in specific heat. This is followed by a rapid rise towards T_L , indicating the enhancement of internal field fluctuations through spin reconfiguration to the canted antiferromagnetic state. It is interesting to note that, below T_L , the λ_{TF} remains constant down to 1.93 K without displaying a sharp fall, persistent spin fluctuations even in the magnetically ordered state, similar to that observed in coupled trillium lattice $\text{K}_2\text{Ni}_2(\text{SO}_4)_3$ [51].

To validate the spin dynamics in the ordered states, ZF- μ SR measurements were performed in the wide temperature range. Figure 6 (d) shows the ZF- μ SR spectra at temperatures above T_L without any change of the initial asymmetry. Furthermore, despite an anomaly in specific heat associated to the magnetic phase transition, the absence of any oscillation or a strong damped signal even in short-time scale, suggests that a dynamical behavior of electronic spins associated with the magnetic phase transition similar to that observed in trillium lattice antiferromagnet $\text{K}_2\text{Ni}_2(\text{SO}_4)_3$. The corresponding μ SR data (Fig. 6) can be well fitted to the phenomenological model $P(t) = A_0 e^{-(\lambda_{\text{ZF}} t)^{\beta_{\text{ZF}}}}$, where A_0 is the initial asymmetry, λ_{ZF} is the muon spin relaxation rate in zero-field and β_{ZF} is the stretched exponent. The estimated relaxation rate exhibits several features as shown in Fig. 6 (b). Upon lowering the temperature from 78 K, the λ_{ZF} remains constant in the temperature range $8 \text{ K} \leq T \leq 78 \text{ K}$. The essentially same behavior is observed by λ_{TF} (see Fig. 5 (b)). Below 8 K, the λ_{ZF} shows a rapid increase, ascribed to the presence of the canted antiferromagnetic phase transition accompanied by a critical slowing down of spin fluctuation consistent with our wTF- μ SR results. The obtained stretched exponent, measuring the distribution of electronic moment, is shown Fig. 6 (c). At high-temperatures, β_{ZF} is close to one, corresponding to fast fluctuation limit. As the temperature decreases, the β_{ZF} value gradually decreases, notably dropping to 0.85 at $T_H \sim 8 \text{ K}$. Below 8 K, the β_{ZF} value gradually decreases, but there is a sudden drop at T_L to a value of 0.6. It is observed that the ZF- μ SR data (for $T \geq 4.41 \text{ K}$) cannot be accurately fitted using a single exponential function ($\beta_{\text{ZF}} = 1$) or models with multi-exponential components [64]. The obtained $\beta_{\text{ZF}} < 1$ is associated with the presence of a distribution of relaxation times, as expected when various spins fluctuate in different timescales due to competing magnetic interactions in KCTPO. The observed β_{ZF} of 0.6 ($> 1/3$) value, as seen in Fig. 6 (c), implies that the splitting in ZFC and FC χ data at 4.3 K is due to canted antiferromagnetic phase rather than spin freezing [80].

Figure 6 (d) displays the time evolution of ZF- μ SR spectra at several temperatures below 4.5 K in the short-time scale. As the temperature decreases below 4.5 K, the polarization initially exhibits a moderate departure from stretched exponential behavior [81]. As it reaches around 1.9 K, it undergoes an abrupt transition into a strongly non-exponential signal. The shorter time domain clearly

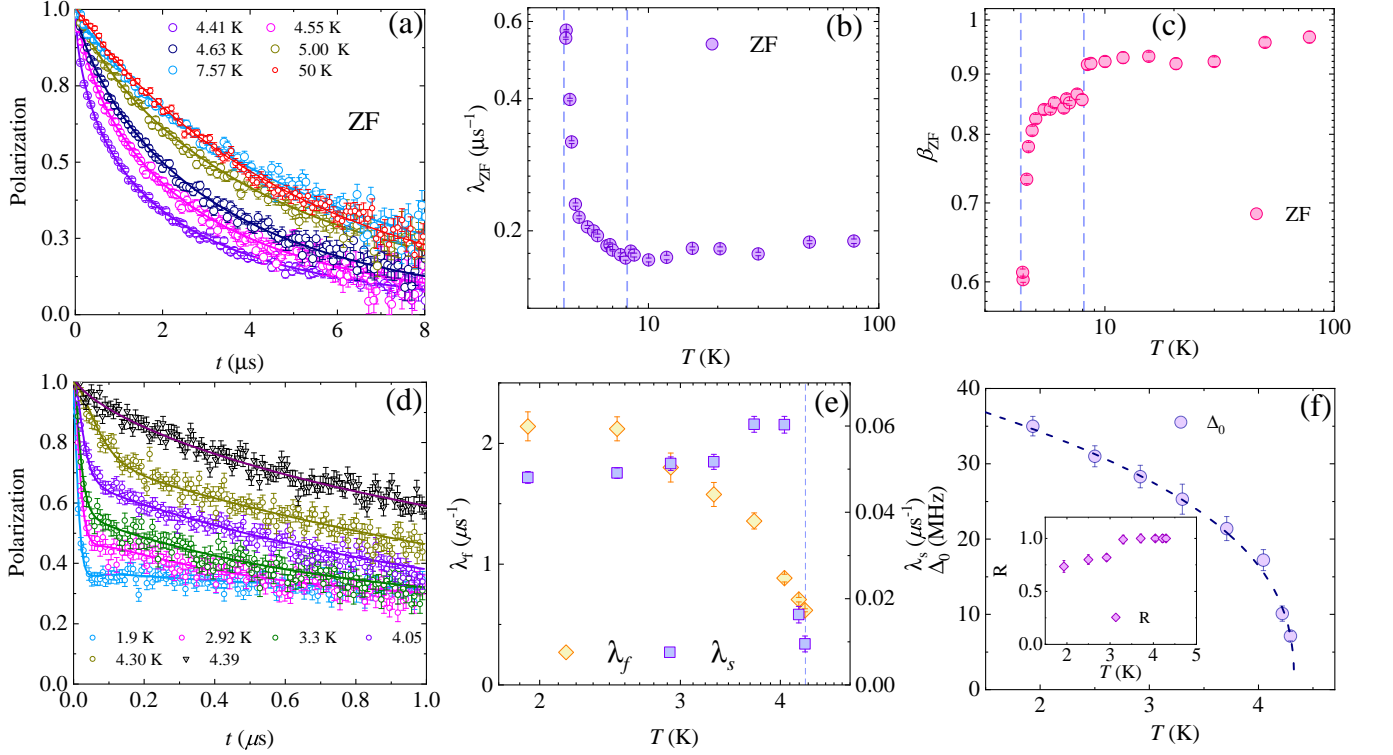


FIG. 6. (a) Time dependence of zero-field μ SR spectra of $\text{K}_2\text{CrTi}(\text{PO}_4)_3$ at temperatures higher than the temperature of canted antiferromagnetic phase transition. The solid lines represent the fitted curve by a stretched exponential function. (b), (c) Temperature dependence of muon spin relaxation rate and stretched exponent as a function of temperature in zero magnetic field on a double logarithmic scale. The dashed vertical bars indicate the position of characteristic transition temperatures at $T_L = 4.30$ K and $T_H = 8$ K. (d) Time evolution of zero-field spectra at temperatures below the canted antiferromagnet state. The solid lines are the fits of Eq. 3 to the data. (e) Temperature dependence of fast (left y-axis) and slow (right y-axis) muon spin relaxation rate on a double logarithmic scale. (f) Mean value of the Gaussian-broadened Gaussian distribution as a function of temperature where the solid lines are the fitted curves with critical scaling behavior of internal field distribution with critical exponent $\beta = 0.37$. Inset shows the temperature dependence of R i.e, the ratio of the width of distributions (W) to the distribution mean (Δ_0).

shows a substantially damped signal, making it challenging to simulate the muon polarization throughout the whole temperature range using a stretched exponential relaxation function. Furthermore, the absence of any peak in the first Fourier transform of the corresponding spectra indicates that the damped signal can not be attributable to coherent oscillations typically observed in long-range ordered magnets [79, 82, 83]. Instead, it suggests the existence of disordered static moments of Cr^{3+} ions below 4.3 K. After attempting with several models [84–86], it turns out that the ZF- μ SR data can be modeled with the following polarization function

$$P_{ZF} = f_z P_{\text{GDG}}(t; \Delta_0, W) e^{-\lambda_s t} + (1 - f_z) e^{-\lambda_f t}, \quad (3)$$

which takes into account a phenomenological Gaussian-broadened Gaussian (GBG) function with a slow exponential decay with relaxation rate λ_s and a fast exponential decay with relaxation rate λ_f [87, 88]. The parameter f_z defines the fraction of Cr^{3+} moments that produce static local fields, while the remaining part contributes to

dynamic fields. The following GBG polarization function

$$P_{\text{GBG}}(t) = \frac{1}{3} + \frac{2}{3} \left(\frac{1}{1 + R^2 \Delta_0^2 t^2} \right)^{3/2} \left(1 - \frac{\Delta_0^2 t^2}{1 + R^2 \Delta_0^2 t^2} \right) \exp \left[-\frac{\Delta_0^2 t^2}{2(1 + R^2 \Delta_0^2 t^2)} \right] \quad (4)$$

is an extension of the Gaussian Kubo-Toyabe function with a Gaussian distribution width W and a mean value Δ_0 , where $R = W/\Delta_0$. This function is commonly employed when the internal field distribution exceeds the Gaussian field distribution. It effectively captures the existence of disordered static magnetic moments with short-range correlations as observed in 3D hyperkagome compound such as $\text{Na}_4\text{Ir}_3\text{O}_8$ which exhibits ZFC and FC splitting in dc susceptibility similar to the compound studied here [24]. The extracted temperature dependence of fast relaxation rate (λ_f ; left y-axis), representing a few fraction of Cr^{3+} moments exhibiting dynamic behavior, and the slow relaxation rate (λ_s ;

right y -axis) corresponds to the remaining fraction Cr^{3+} moments displaying static behavior are shown in Fig. 6 (e). Both λ_f and λ_s start to increase below T_L and attain a constant value at low temperatures indicating the coexistence of static and dynamic components of Cr^{3+} moments in KCTPO.

In KCTPO, the origin of static moments can be associated to the canted antiferromagnetic phase involving a small fraction of static Cr^{3+} moments. Simultaneously, the rest of the Cr^{3+} moments maintain a dynamic state most likely due to the interplay of competing magnetic interactions. In geometrically frustrated magnets, the coexistence of dynamic and static electronic moments is a common scenario, as also observed in two coupled trillium lattice $\text{K}_2\text{Ni}_2(\text{SO}_4)_3$ and pyrochlore lattice $\text{NaCaNi}_2\text{F}_7$ [27]. Δ_0 undergoes an order-parameter-like decrease as the temperature increases from 1.9 K towards T_L . It may be noted that the relative distribution width R steadily increases and reaches a value of one at T_L (inset of Fig. 6 (f)). The critical-like behavior of the local field distribution near T_L is described by phenomenological expression [89, 90]

$\Delta_0(T) = \Delta_0(T = 0 \text{ K}) \left[1 - \frac{T}{T_L}\right]^\beta$ that yields $\beta = 0.37$ that is typical for 3D Heisenberg magnets (see the dashed line in Fig. 6 (f)). Using $\Delta_0 = 35$ MHz at $T = 1.9$ K, the calculated internal magnetic field is found to be $\langle B_{\text{loc}} \rangle \approx 400$ G. In order to confirm such static magnetic field is of electronic origin, we also performed μSR measurements at 3.3 K in longitudinal field (not shown here), which decouples the static field owing to nuclear origin. It is observed that approximately 2 kG $> \langle B_{\text{loc}} \rangle$ longitudinal field is required to recover full polarization, confirming the presence of both dynamic and static moments of Cr^{3+} ions in KCTPO. Similar to KCTPO, the observed muon spin asymmetry of triangular lattice antiferromagnet NiGa_2S_4 was characterized by a stretched exponential function at high temperatures, associated to multichannel relaxation, while the data at low temperatures were primarily influenced by static local fields [81]. The contrasting time evolution of the muon spin polarization function, observed both above and below the characteristic temperature of T_L , may be associated with distinct magnetic phases in KCTPO,

similar to those found in other 3D frustrated magnets [91–94].

IV. CONCLUSION

In summary, we have thoroughly investigated the structural and magnetic properties of nearly perfect $S = 3/2$ trillium lattice $\text{K}_2\text{CrTi}(\text{PO}_4)_3$ through magnetization, specific heat, as well as ESR and μSR techniques. Magnetic susceptibility results suggest that the presence of antiferromagnetic interactions between $S = 3/2$ moments of Cr^{3+} ions. Specific heat measurements unveil two consecutive phase transitions, one at $T_L = 4.3$ K, corresponding to the canted antiferromagnetic phase, and another at $T_H = 8$ K due to an antiferromagnetic phase. Above T_H , the existence of short-range magnetic order is supported by the observation of maximum entropy release and the manifestation of critical-like behavior in the ESR line width. Furthermore, μSR provides concrete evidence of the presence of static and dynamic local magnetic fields, particularly below T_L , as well as a critical slowing down of spin dynamics above T_L and persistent spin dynamics to the lowest temperatures. Further investigations on single crystals is essential to gain a detailed understanding of the low-energy excitations associated to the short range order above the transition temperature and the multi-stage spin dynamics in this three-dimensional frustrated antiferromagnet.

ACKNOWLEDGMENTS

P.K. acknowledges the funding by the Science and Engineering Research Board, and Department of Science and Technology, India through Research Grants. The work at SKKU was supported by the National Research Foundation (NRF) of Korea (Grant no. RS-2023-00209121, 2020R1A5A1016518). We further acknowledge the support of HLD at HZDR, member of the European Magnetic Field Laboratory (EMFL).

-
- [1] L. Balents, *Nature* **464**, 199 (2010).
 [2] N. D. Mermin and H. Wagner, *Phys. Rev. Lett.* **17**, 1133 (1966).
 [3] P. Khuntia, *J. Magn. Magn. Mater.* **489**, 165435 (2019).
 [4] J. Khatua, B. Sana, A. Zorko, M. Gomilšek, K. Sethupathi, M. R. Rao, M. Baenitz, B. Schmidt, and P. Khuntia, *Phys. Rep.* **1041**, 1 (2023).
 [5] Y. Zhou, K. Kanoda, and T.-K. Ng, *Rev. Mod. Phys.* **89**, 025003 (2017).
 [6] J. Wen, S.-L. Yu, S. Li, W. Yu, and J.-X. Li, *npj Quantum Mater.* **4**, 12 (2019).
 [7] L. Savary and L. Balents, *Rep. Prog. Phys.* **80**, 016502 (2016).
 [8] C. Broholm, R. J. Cava, S. A. Kivelson, D. G. Nocera, M. R. Norman, and T. Senthil, *Science* **367**, eaay0668 (2020).
 [9] P. W. Anderson, *Mater. Res. Bull.* **8**, 153 (1973).
 [10] X. G. Wen, *Phys. Rev. B* **44**, 2664 (1991).
 [11] G. Baskaran, Z. Zou, and P. Anderson, *Solid State Commun.* **63**, 973 (1987).
 [12] P. W. Anderson, *science* **235**, 1196 (1987).
 [13] H.-C. Jiang and S. A. Kivelson, *Phys. Rev. Lett.* **127**, 097002 (2021).

- [14] E. Fradkin, S. A. Kivelson, and J. M. Tranquada, *Rev. Mod. Phys.* **87**, 457 (2015).
- [15] C. Castelnovo, R. Moessner, and S. Sondhi, *Annual Review of Condensed Matter Physics* **3**, 35 (2012).
- [16] C. Nayak, S. H. Simon, A. Stern, M. Freedman, and S. Das Sarma, *Rev. Mod. Phys.* **80**, 1083 (2008).
- [17] P. W. Phillips, L. Yeo, and E. W. Huang, *Nature Physics* **16**, 1175 (2020).
- [18] B. Göbel, I. Mertig, and O. A. Tretiakov, *Phys. Rep.* **895**, 1 (2021), beyond skyrmions: Review and perspectives of alternative magnetic quasiparticles.
- [19] S. Jeon, D. Wulferding, Y. Choi, S. Lee, K. Nam, K. H. Kim, M. Lee, T.-H. Jang, J.-H. Park, S. Lee, S. Choi, C. Lee, H. Nojiri, and K.-Y. Choi, (2023), [arXiv:2311.11619 \[cond-mat.str-el\]](https://arxiv.org/abs/2311.11619).
- [20] T. Arh, B. Sana, M. Pregelj, P. Khuntia, Z. Jagličić, M. D. Le, P. K. Biswas, P. Manuel, L. Mangin-Thro, A. Ozarowski, and A. Zorko, *Nat. Mater.* **21**, 416 (2022).
- [21] P. Khuntia, F. Bert, P. Mendels, B. Koteswararao, A. V. Mahajan, M. Baenitz, F. C. Chou, C. Baines, A. Amato, and Y. Furukawa, *Phys. Rev. Lett.* **116**, 107203 (2016).
- [22] S. Chillal, Y. Iqbal, H. O. Jeschke, J. A. Rodriguez-Rivera, R. Bewley, P. Manuel, D. Khalyavin, P. Steffens, R. Thomale, A. T. M. N. Islam, J. Reuther, and B. Lake, *Nat. Commun.* **11**, 2348 (2020).
- [23] A. C. Shockley, F. Bert, J.-C. Orain, Y. Okamoto, and P. Mendels, *Phys. Rev. Lett.* **115**, 047201 (2015).
- [24] R. Dally, T. Hogan, A. Amato, H. Luetkens, C. Baines, J. Rodriguez-Rivera, M. J. Graf, and S. D. Wilson, *Phys. Rev. Lett.* **113**, 247601 (2014).
- [25] K. W. Plumb, H. J. Changlani, A. Scheie, S. Zhang, J. W. Krizan, J. A. Rodriguez-Rivera, Y. Qiu, B. Winn, R. J. Cava, and C. L. Broholm, *Nat. Phys.* **15**, 54 (2019).
- [26] J. W. Krizan and R. J. Cava, *Phys. Rev. B* **92**, 014406 (2015).
- [27] Y. Cai, M. N. Wilson, A. M. Hallas, L. Liu, B. A. Frandsen, S. R. Dunsiger, J. W. Krizan, R. J. Cava, O. Rubel, Y. J. Uemura, and G. M. Luke, *J. Condens. Matter Phys.* **30**, 385802 (2018).
- [28] B. Gao, T. Chen, D. W. Tam, C.-L. Huang, K. Sasmal, D. T. Adroja, F. Ye, H. Cao, G. Sala, M. B. Stone, C. Baines, J. A. T. Verzhak, H. Hu, J.-H. Chung, X. Xu, S.-W. Cheong, M. Nallaiyan, S. Spagna, M. B. Maple, A. H. Nevidomskyy, E. Morosan, G. Chen, and P. Dai, *Nat. Phys.* **15**, 1052 (2019).
- [29] J. Khatua, S. Bhattacharya, Q. P. Ding, S. Vrtnik, A. M. Strydom, N. P. Butch, H. Luetkens, E. Kermarrec, M. S. R. Rao, A. Zorko, Y. Furukawa, and P. Khuntia, *Phys. Rev. B* **106**, 104404 (2022).
- [30] C. Broholm, R. J. Cava, S. A. Kivelson, D. G. Nocera, M. R. Norman, and T. Senthil, *Science* **367** (2020).
- [31] S. Kivelson and S. Sondhi, *Nat. Rev. Phys.* **5**, 368 (2023).
- [32] T. Lancaster, *Contemp. Phys.* **0**, 1 (2023).
- [33] J. Khatua, M. Gomilšek, J. C. Orain, A. M. Strydom, Z. Jagličić, C. V. Colin, S. Petit, A. Ozarowski, L. Mangin-Thro, K. Sethupathi, M. S. R. Rao, A. Zorko, and P. Khuntia, *Commun. Phys.* **5**, 99 (2022).
- [34] L. T. Nguyen and R. J. Cava, *Chemical Reviews* **121**, 2935 (2021).
- [35] C. Bradley and A. Cracknell, *The mathematical theory of symmetry in solids: representation theory for point groups and space groups* (Oxford University Press, 2010).
- [36] M. Kakihana, K. Nishimura, Y. Ashitomi, T. Yara, D. Aoki, A. Nakamura, F. Honda, M. Nakashima, Y. Amako, Y. Uwatoko, T. Sakakibara, S. Nakamura, T. Takeuchi, Y. Haga, E. Yamamoto, H. Harima, M. Hedo, T. Nakama, and Y. Ōnuki, *Journal of Electronic Materials* **46**, 3572 (2017).
- [37] T. E. Redpath and J. M. Hopkinson, *Phys. Rev. B* **82**, 014410 (2010).
- [38] V. A. Chizhikov and V. E. Dmitrienko, *Phys. Rev. B* **88**, 214402 (2013).
- [39] I. Dzyaloshinskii, *Sov. Phys. JETP* **19**, 960 (1964).
- [40] L. Ding, X. Xu, H. O. Jeschke, X. Bai, E. Feng, A. S. Alemayehu, J. Kim, F.-T. Huang, Q. Zhang, X. Ding, N. Harrison, V. Zapf, D. Khomskii, I. I. Mazin, S.-W. Cheong, and H. Cao, *Nat. Commun.* **12**, 5339 (2021).
- [41] M. Ramakrishnan, E. Constable, A. Cano, M. Mostovoy, J. S. White, N. Gurung, E. Schierle, S. d. Brion, C. V. Colin, F. Gay, P. Lejay, E. Ressouche, E. Weschke, V. Scagnoli, R. Ballou, V. Simonet, and U. Staub, *npj Quantum Materials* **4**, 60 (2019).
- [42] Y. A. Izyumov, *Soviet Physics Uspekhi* **27**, 845 (1984).
- [43] F. Qian, L. J. Bannenberg, H. Wilhelm, G. Chaboussant, L. M. Debeer-Schmitt, M. P. Schmidt, A. Aqeel, T. T. M. Palstra, E. Brück, A. J. E. Lefering, C. Pappas, M. Mostovoy, and A. O. Leonov, *Science Advances* **4**, eaat7323 (2018).
- [44] S. Mühlbauer, B. Binz, F. Jonietz, C. Pfleiderer, A. Rosch, A. Neubauer, R. Georgii, and P. Böni, *Science* **323**, 915 (2009).
- [45] X. Z. Yu, N. Kanazawa, Y. Onose, K. Kimoto, W. Z. Zhang, S. Ishiwata, Y. Matsui, and Y. Tokura, *Nat. Mater.* **10**, 106 (2011).
- [46] N. Kanazawa, Y. Onose, T. Arima, D. Okuyama, K. Ohoyama, S. Wakimoto, K. Kakurai, S. Ishiwata, and Y. Tokura, *Phys. Rev. Lett.* **106**, 156603 (2011).
- [47] N. Higa, T. U. Ito, M. Yogi, T. Hattori, H. Sakai, S. Kambe, Z. Guguchia, W. Higemoto, M. Nakashima, Y. Homma, A. Nakamura, F. Honda, Y. Shimizu, D. Aoki, M. Kakihana, M. Hedo, T. Nakama, Y. Ōnuki, and Y. Tokunaga, *Phys. Rev. B* **104**, 045145 (2021).
- [48] F. Kneidinger, I. Zeiringer, A. Siderenko, E. Bauer, H. Michor, P. Rogl, and J. G. Sereni, *Phys. Rev. B* **100**, 134442 (2019).
- [49] C. Pfleiderer, G. J. McMullan, S. R. Julian, and G. G. Lonzarich, *Phys. Rev. B* **55**, 8330 (1997).
- [50] J. M. Hopkinson and H.-Y. Kee, *Phys. Rev. B* **74**, 224441 (2006).
- [51] I. Živković, V. Favre, C. Salazar Mejia, H. O. Jeschke, A. Magrez, B. Dabholkar, V. Nocolak, R. S. Freitas, M. Jeong, N. G. Hegde, L. Testa, P. Babkevich, Y. Su, P. Manuel, H. Luetkens, C. Baines, P. J. Baker, J. Wosnitza, O. Zaharko, Y. Iqbal, J. Reuther, and H. M. Rønnow, *Phys. Rev. Lett.* **127**, 157204 (2021).
- [52] W. Yao, Q. Huang, T. Xie, A. Podlesnyak, A. Brassington, C. Xing, R. S. D. Mudiyansele, H. Wang, W. Xie, S. Zhang, M. Lee, V. S. Zapf, X. Bai, D. A. Tennant, J. Liu, and H. Zhou, *Phys. Rev. Lett.* **131**, 146701 (2023).
- [53] K. Boya, K. Nam, K. Kargeti, A. Jain, R. Kumar, S. K. Panda, S. M. Yusuf, P. L. Paulose, U. K. Voma, E. Kermarrec, K. H. Kim, and B. Koteswararao, *APL Materials* **10**, 101103 (2022).
- [54] J. M. Bulled, J. A. M. Paddison, A. Wildes, E. Lhotel, S. J. Cassidy, B. Pato-Doldán, L. C. Gómez-Aguirre, P. J. Saines, and A. L. Goodwin, *Phys. Rev. Lett.* **128**, 177201 (2022).

- (2022).
- [55] X. Huai and T. T. Tran, *Annu. Rev. Mater. Res.* **53**, 253 (2023).
- [56] A. E. Hall, P. Manuel, D. D. Khalyavin, F. Orlandi, D. A. Mayoh, L.-J. Chang, Y.-S. Chen, D. G. C. Jonas, M. R. Lees, and G. Balakrishnan, *Phys. Rev. Mater.* **7**, 114402 (2023).
- [57] A. Suter and B. Wojek, *Phys. Procedia* **30**, 69 (2012), 12th International Conference on Muon Spin Rotation, Relaxation and Resonance (μ SR2011).
- [58] B. H. Toby, *J. Appl. Crystallogr.* **34**, 210 (2001).
- [59] J. Isasi and A. Daidouh, *Solid State Ion.* **133**, 303 (2000).
- [60] A. Boudjada and R. Perret, *J. Appl. Crystallogr.* **10**, 129 (1977).
- [61] S. T. Norberg, *Acta Crystallographica Section B* **58**, 743 (2002).
- [62] S. V. Isakov, J. M. Hopkinson, and H.-Y. Kee, *Phys. Rev. B* **78**, 014404 (2008).
- [63] M. S. Khan, A. Bandyopadhyay, A. Nag, V. Kumar, A. V. Mahajan, and S. Ray, *Phys. Rev. B* **100**, 064423 (2019).
- [64] S. Lee, T. Zhu, Y. Oshima, T. Shiroka, C. Wang, H. Luetkens, H. Yang, M. Lü, and K.-Y. Choi, *Phys. Rev. B* **105**, 094439 (2022).
- [65] T. Zhu, S. Lee, X. Zhang, H. Yang, Y. Jin, Y. Jin, K.-Y. Choi, and M. Lü, *Inorg. Chem.* **60**, 13707 (2021).
- [66] Z. Bukowski, D. Rybicki, M. Babij, J. Przewoźnik, L. Gondek, J. Żukrowski, and C. Kapusta, *Sci. Rep.* **12**, 14718 (2022).
- [67] Y. Lai, L. Ke, J. Yan, R. D. McDonald, and R. J. McQueeney, *Phys. Rev. B* **103**, 184429 (2021).
- [68] G. Cao, A. Subedi, S. Calder, J.-Q. Yan, J. Yi, Z. Gai, L. Poudel, D. J. Singh, M. D. Lumsden, A. D. Christianson, B. C. Sales, and D. Mandrus, *Phys. Rev. B* **87**, 155136 (2013).
- [69] A. Verrier, F. Bert, J. M. Parent, M. El-Amine, J. C. Orain, D. Boldrin, A. S. Wills, P. Mendels, and J. A. Quilliam, *Phys. Rev. B* **101**, 054425 (2020).
- [70] B. Schmidt and P. Thalmeier, *Phys. Rep.* **703**, 1 (2017), frustrated two dimensional quantum magnets.
- [71] S. Kimura, S. Imajo, M. Gen, T. Momoi, M. Hagiwara, H. Ueda, and Y. Kohama, *Phys. Rev. B* **105**, L180405 (2022).
- [72] J. Khatua, T. Arh, S. B. Mishra, H. Luetkens, A. Zorko, B. Sana, M. S. R. Rao, B. R. K. Nanda, and P. Khuntia, *Sci. Rep.* **11**, 6959 (2021).
- [73] G. S. Murugan, C. Lee, R. Kalaivanan, I. P. Muthuselvam, Y. Oshima, K.-Y. Choi, and R. Sankar, *Phys. Rev. B* **107**, 214411 (2023).
- [74] A. Abragam and B. Bleaney, *Electron paramagnetic resonance of transition ions* (Clarendon Press, Oxford, 1970).
- [75] A. Glamazda, Y. S. Choi, S.-H. Do, S. Lee, P. Lemmens, A. N. Ponomaryov, S. A. Zvyagin, J. Wosnitzer, D. P. Sari, I. Watanabe, and K.-Y. Choi, *Phys. Rev. B* **95**, 184430 (2017).
- [76] S. Lee, S.-H. Do, W.-J. Lee, Y. S. Choi, M. Lee, E. S. Choi, A. P. Reyes, P. L. Kuhns, A. Ozarowski, and K.-Y. Choi, *Phys. Rev. B* **93**, 174402 (2016).
- [77] A. Yaouanc and P. D. De Reotier, *Muon spin rotation, relaxation, and resonance: applications to condensed matter*, 147 (OUP Oxford, 2011).
- [78] E. Nocerino, S. Kobayashi, C. Witteveen, O. K. Forslund, N. Matsubara, C. Tang, T. Matsukawa, A. Hoshikawa, A. Koda, K. Yoshimura, I. Umegaki, Y. Sassa, F. O. von Rohr, V. Pomjakushin, J. H. Brewer, J. Sugiyama, and M. Månsson, *Commun. Mater.* **4**, 81 (2023).
- [79] K. Papadopoulos, O. K. Forslund, E. Nocerino, F. O. L. Johansson, G. Simutis, N. Matsubara, G. Morris, B. Hitti, D. Arseneau, P. Svedlindh, M. Medarde, D. Andreica, J.-C. Orain, V. Pomjakushin, L. Börjesson, J. Sugiyama, M. Månsson, and Y. Sassa, *Phys. Rev. B* **106**, 214410 (2022).
- [80] I. A. Campbell, A. Amato, F. N. Gygax, D. Herlach, A. Schenck, R. Cywinski, and S. H. Kilcoyne, *Phys. Rev. Lett.* **72**, 1291 (1994).
- [81] A. Yaouanc, P. Dalmas de Réotier, Y. Chapuis, C. Marin, G. Lapertot, A. Cervellino, and A. Amato, *Phys. Rev. B* **77**, 092403 (2008).
- [82] C. Koo, J. Werner, M. Tzschoppe, M. Abdel-Hafiez, P. K. Biswas, R. Sarkar, H.-H. Klauss, G. V. Raganyan, E. A. Ovchencov, A. Y. Nikulin, A. N. Vasiliev, E. A. Zvereva, and R. Klingeler, *Phys. Rev. B* **97**, 224416 (2018).
- [83] T. Weinhold, C. Wang, F. Seewald, V. Grinenko, Y. Imai, F. Sato, K. Ohgushi, H. H. Klauss, and R. Sarkar, “Magnetism in kitaev quantum spin liquid candidate ruBr_3 ,” (2023), [arXiv:2311.03800 \[cond-mat.str-el\]](https://arxiv.org/abs/2311.03800).
- [84] Y. Li, Q.-Y. Li, W. Li, T. Liu, D. J. Vonshen, P. K. Biswas, and D. Adroja, *npj Quantum Materials* **6**, 34 (2021).
- [85] P. Khuntia, S. Manni, F. R. Foronda, T. Lancaster, S. J. Blundell, P. Gegenwart, and M. Baenitz, *Phys. Rev. B* **96**, 094432 (2017).
- [86] A. Zorko, F. Bert, P. Mendels, K. Marty, and P. Bordet, *Phys. Rev. Lett.* **104**, 057202 (2010).
- [87] D. R. Noakes and G. M. Kalvius, *Phys. Rev. B* **56**, 2352 (1997).
- [88] S.-H. Do, W.-J. Lee, S. Lee, Y. S. Choi, K.-J. Lee, D. I. Gorbunov, J. Wosnitzer, B. J. Suh, and K.-Y. Choi, *Phys. Rev. B* **98**, 014407 (2018).
- [89] S. Lee, Y. S. Choi, S.-H. Do, W. Lee, C. H. Lee, M. Lee, M. Vojta, C. N. Wang, H. Luetkens, Z. Guguchia, and K.-Y. Choi, *Nat. Commun.* **14**, 7405 (2023).
- [90] P. J. Baker, I. Franke, F. L. Pratt, T. Lancaster, D. Prabhakaran, W. Hayes, and S. J. Blundell, *Phys. Rev. B* **84**, 174403 (2011).
- [91] O. K. Forslund, K. Papadopoulos, E. Nocerino, G. Morris, B. Hitti, D. Arseneau, V. Pomjakushin, N. Matsubara, J.-C. Orain, P. Svedlindh, D. Andreica, S. Jana, J. Sugiyama, M. Månsson, and Y. Sassa, *Phys. Rev. B* **102**, 144409 (2020).
- [92] J. A. Hodges, P. Bonville, A. Forget, A. Yaouanc, P. Dalmas de Réotier, G. André, M. Rams, K. Królas, C. Ritter, P. C. M. Gubbens, C. T. Kaiser, P. J. C. King, and C. Baines, *Phys. Rev. Lett.* **88**, 077204 (2002).
- [93] S. Lee, S.-H. Do, W. Lee, Y. S. Choi, J. van Tol, A. P. Reyes, D. Gorbunov, W.-T. Chen, and K.-Y. Choi, *npj Quantum Materials* **6**, 47 (2021).
- [94] B. A. Frandsen, K. A. Petersen, N. A. Ducharme, A. G. Shaw, E. J. Gibson, B. Winn, J. Yan, J. Zhang, M. E. Manley, and R. P. Hermann, *Phys. Rev. Mater.* **4**, 074405 (2020).